Published in final edited form as:

AJR Am J Roentgenol. 2017 December ; 209(6): 1216–1227. doi:10.2214/AJR.17.17857.

Computer-Aided Diagnosis of Ground-Glass Opacity Nodules Using Open-Source Software for Quantifying Tumor Heterogeneity

Ming Li[1], **Vivek Narayan**[2], **Ritu R. Gill**[3], **Jyothi P. Jagannathan**[4], **Maria F. Barile**[3], **Feng Gao**[1], **Raphael Bueno**[5], and **Jagadeesan Jayender**[3]

[1]Department of Radiology, HuaDong Hospital, Fudan University, Shanghai, China

[2]Dana Farber Cancer Institute, Boston, MA

[3]Department of Radiology, Brigham and Women's Hospital, Harvard Medical School, 75 Francis St, L1-050, Boston, MA 02115. Address correspondence to J. Jayender (jayender@bwh.harvard.edu)

[4]Department of Radiology, Dana Farber Cancer Institute, Harvard Medical School, Boston, MA

[5]Department of Surgery, Brigham and Women's Hospital, Harvard Medical School, Boston, MA

Abstract

OBJECTIVE—The purposes of this study are to develop quantitative imaging biomarkers obtained from high-resolution CTs for classifying ground-glass nodules (GGNs) into atypical adenomatous hyperplasia (AAH), adenocarcinoma in situ (AIS), minimally invasive adenocarcinoma (MIA), and invasive adenocarcinoma (IAC); to evaluate the utility of contrast enhancement for differential diagnosis; and to develop and validate a support vector machine (SVM) to predict the GGN type.

MATERIALS AND METHODS—The heterogeneity of 248 GGNs was quantified using custom software. Statistical analysis with a univariate Kruskal-Wallis test was performed to evaluate metrics for significant differences among the four GGN groups. The heterogeneity metrics were used to train a SVM to learn and predict the lesion type.

RESULTS—Fifty of 57 and 51 of 57 heterogeneity metrics showed statistically significant differences among the four GGN groups on unenhanced and contrast-enhanced CT scans, respectively. The SVM predicted lesion type with greater accuracy than did three expert radiologists. The accuracy of classifying the GGNs into the four groups on the basis of the SVM algorithm was 70.9%, whereas the accuracy of the radiologists was 39.6%. The accuracy of SVM in classifying the AIS and MIA nodules was 73.1%, and the accuracy of the radiologists was 35.7%. For indolent versus invasive lesions, the accuracy of the SVM was 88.1%, and the accuracy of the radiologists was 60.8%. We found that contrast enhancement does not significantly improve the differential diagnosis of GGNs.

Based on a presentation at the Radiological Society of North America 2015 annual meeting, Chicago, IL.

CONCLUSION—Compared with the GGN classification done by the three radiologists, the SVM trained regarding all the heterogeneity metrics showed significantly higher accuracy in classifying the lesions into the four groups, differentiating between AIS and MIA and between indolent and invasive lesions. Contrast enhancement did not improve the differential diagnosis of GGNs.

Keywords

computer-aided diagnosis; ground-glass opacity lesions; imaging biomarkers; International Association for the Study of Lung Cancer guidelines

Lung cancer is the leading cause of cancer-related deaths worldwide. The National Cancer Institute estimates that there will be 221,200 new cases of lung cancer in 2015, with 158,000 deaths due to lung cancer. The introduction of low-dose screening CT has led to early detection of small lung adenocarcinoma, with a significant decrease in death due to lung cancer [1, 2]. On CT screening examinations, nodules appear as solid, part-solid, or nonsolid lesions, with a significant portion of part-solid and nonsolid lesions identified as malignant.

To address the problem of accurately classifying lung nodules, in 2011, the International Association for the Study of Lung Cancer (IASLC), the American Thoracic Society, and the European Respiratory Society proposed a new lung adenocarcinoma classification [3] according to which GGNs are classified as atypical adenomatous hyperplasia (AAH), adenocarcinoma in situ (AIS), minimally invasive adenocarcinoma (MIA), or invasive adenocarcinoma (IAC) on the basis of the size of the lesion and the presence of a solid component on pathologic analysis. The new classification has had a significant impact on patient therapy options and followup because prognosis varies widely among the different pathologic subtypes [4, 5]. Recent studies have shown that patients with early-stage AIS and MIA have a disease-free survival rate of almost 100%, whereas patients with IACs have a disease-free survival rate of 60–70% [6–9]. Therefore, it is crucial to determine the risk of lesion malignancy accurately on diagnostic CT examination, to enable early intervention. Although CT images have been shown to identify the pathologic invasiveness of lung lesions [10], it is not clear how the 2011 lesion classification guidelines can be translated into imaging findings on diagnostic CT examinations [11–14].

The three objectives of the present study are to develop and validate quantitative imaging biomarkers obtained from high-resolution CT examinations for classifying GGNs as AAH, AIS, MIA, or IAC; to evaluate the utility of contrast enhancement for differential diagnosis of the lesions; and develop and to validate a machine learning algorithm based on the support vector machine (SVM) for predicting the GGN type. Analysis was performed using open-source software that was developed for quantifying tumor heterogeneity, which is expected to encourage other users to validate the imaging biomarkers with the use of a standardized set of quantification tools.

Materials and Methods

Software Module

An open-source software module, HeterogeneityCAD, was developed as part of the image processing and navigation software 3D Slicer (version 4.3.0, Brigham and Women's

Hospital) [15]. The module was developed in the programming language Python (version 4.3.0, Python Software, Brigham and Women's Hospital) and uses a cross-platform application framework for designing the user interface (Qt, version 4.8.7, Qt). The module allows the easy input of the 3D image volume and the label map that defines the ROI to be analyzed. Typically, the ROI outlines the tumor on diagnostic imaging. The image volume could be from MRI, CT, or PET/CT examinations or from parameter maps derived from pharmacokinetic models that analyze contrast perfusion. The module quantifies the heterogeneity of the ROI with the use of 57 metrics that are subdivided into first-order statistics, shape and morphologic metrics, texture metrics, geometric metrics, and Rényi dimensions. First-order statistics include minimum, maximum, and mean signal intensity values within the ROI, skewness, variance, and kurtosis. Shape and morphologic metrics include volume, surface area, compactness, and maximum 3D diameter. The texture metrics are derived from the gray-level co-occurrence matrix (GLCM) and the gray-level run-length (GLRL) matrix. The metrics quantify the texture or coarseness of the ROI. The Rényi metrics assume that the ROI is a fractal, and box counting and Rényi dimensions are computed. A full list of metrics and their definitions are provided at [16]. The module can also be run from the command line to enable batch processing of tumor volumes and label maps.

Patient Selection

The study was HIPAA compliant and was approved by an institutional review board. Informed consent was waived because the study is retrospective.

A total of 235 patients (93 men [age, 30–76 years] and 142 women [age, 31–77 years]) were included in this study. The patients had a total of 248 lesions, including AAH ($n = 17$), AIS ($n = 73$), MIA ($n = 99$), and IAC ($n = 59$). Lesions included solid, part-solid, and pure ground-glass opacity nodules (GGNs) that were less than 30 mm in diameter on preoperative CT evaluation.

All patients underwent diagnostic preoperative CT, in addition to lung surgery. Of the 235 patients (248 nodules), 109 patients (122 nodules) also were administered contrast material and underwent postoperative CT, which resulted in the diagnosis of AAH ($n = 7$), AIS ($n = 49$), MIA ($n = 39$), and IAC ($n = 27$). In addition, all patients underwent segmentectomy or lobectomy via video-assisted thoracic surgery, and the pathologic finding for the lesion served as the reference standard. No patient had a previous primary lung tumor.

CT Technique

The area covered by the chest CT examination extended from the apex to the base of the lung, including the chest wall and axillary fossa. The first dataset, which consisted of preoperative and postoperative CT scans of 122 nodules, was acquired using a 64-MDCT system (GE LightSpeed VCT or GE Discovery CT750 HD, GE Healthcare), with use of the following parameters: section width, 1.25 mm; reconstruction interval, 1.25 mm; pitch, 0.984; tube voltage, 120 kV; tube current, 250 mA; display FOV, 28 × 28 cm to 36 × 36 cm; matrix size, 512 × 512; and pixel size, 0.55–0.7 mm. All patients received a bolus of 80–100 mL of IV contrast medium (350 mg I/mL; Optiray, Mallinckrodt) administered at a rate of

3–4 mL/s with the use of a power injector via an 18- or 20-gauge cannula in an antecubital vein. The postoperative CT scan was acquired 60 seconds after the administration of contrast medium. Both standard and high-resolution reconstruction kernels were used for image reconstructions. The second dataset, which consisted only of unenhanced CT images of 126 nodules, was acquired using either a 16-MDCT system (Sensation 16, Siemens Healthcare) with use of a section width of 1 mm, a reconstruction interval of 1 mm, pitch of 1, tube voltage of 120 kV, and tube current of 150 mA or a 64-MDCT system (GE Discovery CT750 HD, GE Healthcare) with use of the same parameters used for preoperative CT.

Image Analysis

The CT images, which were obtained in DICOM format, were loaded in the image processing and navigation software. A chest radiologist with 16 years of experience delineated the lesion on preoperative and postoperative CT images. A threshold was initially set to differentiate the nodule from the surrounding parenchyma. After visual confirmation that the nodule was included, the user confirmed the choice of the signal intensity threshold for painting around the nodule. Using the threshold paint option, the nodule was segmented on preoperative CT and postoperative CT images. Care was taken to ensure that the vessels were not included in the segmentation mask. The CT volume and the segmentation mask were then provided to the software module. The heterogeneity metrics were computed for the segmented lesions on preoperative and postoperative CT. The heterogeneity metrics were saved and statistically analyzed for the four GGN groups.

Support Vector Machine

An SVM has been developed that uses heterogeneity metrics for predicting the GGN type [17–19]. The SVM algorithm learns and predicts the complex nonlinear mapping from the 57-tuple vector consisting of the heterogeneity metrics (i.e., the input variable) to the lesion type (i.e., the output variable). To avoid numeric inaccuracies and problems with a large range of values for the parameters, the 57-tuple input vector for the training set is first scaled so that each of the elements of the vector lies between 0 and 1. A radial basis function (RBF) kernel is used to design the SVM so as to separate the 57-tuple vector with use of a complex decision boundary based on the lesion type. The RBF kernel nonlinearly maps input samples into a higher dimensional space. The RBF kernel has a form similar to that of a gaussian kernel and has two parameters that need to be optimized: a penalty factor for the error term (C) and a free parameter for the RBF (γ). We performed an N-fold cross-validation by first dividing the training set into N equally distributed subsets to determine the optimal C and γ parameters. The SVM was then sequentially trained on the $N - 1$ subsets and was tested on the one remaining subset. A grid search using exponentially growing values was used to sequentially choose (C, γ) pairs. The (C, γ) pair that provided the best cross-validation accuracy was chosen for the trained SVM. The dataset was divided into training and testing phases in which 80% of the samples were used for training the SVM and the remaining 20% of the samples were used for testing the SVM.

Manual Classification of the Lesion

Three expert chest radiologists categorized the lesions on the basis of the new classification of lung adenocarcinoma published in 2011 [3]. Each case was loaded in image processing and navigation software with the lung window settings (width, 1400; level, −500) so as to highlight the lesions. The software provided the user with the option of measuring the size of the lesion and the size of the solid component used in classification of the lesion. The expert radiologists classified the lesions sequentially on preoperative and postoperative CT.

Statistical Analysis

All four classes—The metrics computed on preoperative and postoperative CT were compared for all four classes (AAH, AIS, MIA, and IAC) with use of the univariate Kruskal-Wallis test. A $p < 0.05$ was considered to denote statistical significance.

Adenocarcinoma in situ versus minimally invasive adenocarcinoma—The heterogeneity on preoperative and postoperative CT was compared for the AIS and MIA categories with use of the Mann-Whitney test because the metrics were assumed to be nonnormally distributed.

Indolent versus invasive lesions—With AAH and AIS considered indolent carcinomas, and with MIA and IAC considered invasive carcinomas, the metrics computed from preoperative and postoperative CT were compared for the two groups with use of the Mann-Whitney statistical test, under the assumption that the metrics were nonnormally distributed.

Support vector machine prediction—The output of the SVM, which predicts lesion type, was compared with the pathologic results. The accuracy of predicting the lesions by the SVM was then computed.

Radiologists' prediction—The lesion type predicted by the three radiologists was compared with the ground-truth classification obtained from pathologic analysis. The accuracy of manual classification of the lesions was computed for preoperative and postoperative CT examinations.

Interrater reliability—The Fleiss kappa value was also calculated to evaluate the interrater reliability. A kappa value of 1 implies perfect agreement, whereas values of less than 1 imply less than perfect agreement. The agreement categories used in the study were defined as follows: poor agreement, $\kappa \leq 0.20$; fair agreement, $0.21 < \kappa \leq 0.40$; moderate agreement, $0.41 < \kappa \leq 0.60$; good agreement, $0.61 < \kappa \leq 0.80$; and very good agreement, $0.81 < \kappa \leq 1.00$. All statistical analyses were conducted using Matlab software (version 2013b, MathWorks).

Results

Three-Dimensional Slicer Module

Figure 1 shows the layout for the module in the image processing and navigation software. The module allows easy input of the DICOM volume and the segmented lesion label map for quantifying tumor heterogeneity. The various subpanels within the module show the heterogeneity metrics that have been selected for computation. When the metrics have been computed, the user has the option of saving the metrics for further statistical analysis.

Statistical Analysis of Tumor Heterogeneity Metrics on Preoperative CT

Figure 2 shows the preoperative CT images for the four types of GGNs. Subtle changes in the lesion appearance on CT differentiate the four types of GGNs. The summary statistics for representative heterogeneity metrics are listed in Table 1. Of the 57 metrics that were computed for the segmented tumor on preoperative CT, 50 metrics showed significant differences for the four types of GGNs. In order of decreasing significance, the metrics that showed maximum differentiation between the four lesion groups were maximum signal intensity, variance of the signal intensity values, variance in the GLCM, autocorrelation, and the number of gray levels. The mean signal intensity (expressed as Hounsfield units) for the four lesion groups was as follows: for AAH, −805.3 HU; for AIS, −806.3 HU; for MIA, −785.7 HU; and for IAC, −736.6 HU. The increasing signal intensity values for the four lesion groups are directly related to the increasing size of the solid component of the lesions, although the mean signal intensities of the AAH and AIS groups are similar. Among the four groups, there is greater differentiation in maximum signal intensity, which, again, is caused by the increased size of the solid component of the lesion. Mean entropy, a measure of disorder, increases from AAH to IAC lesions as follows: for AAH, 1772.7; for AIS, 2696; for MIA, 6081; and for IAC, 22,019; these findings confirm that IAC lesions have a more disorganized structure than AAH, AIS, or MIA lesions.

The mean volumes (25th and 75th percentiles) of the four lesion groups were as follows: for AAH, 0.43 mL (0.11 and 0.32 mL); for AIS, 0.53 mL (0.18 and 0.47 mL); for MIA, 0.94 mL (0.27 and 1.08 mL); and for IAC, 2.10 mL (0.53 and 2.23 mL). The mean maximum 3D diameters (25th and 75th percentiles) of the GGNs were as follows: for AAH, 12.0 mm (8.31 and 12.11 mm); for AIS, 13.7 mm (10.14 and 14.11 mm); for MIA, 16.1 mm (11.55 and 21.05 mm); and for IAC, 22.5 mm (14.92 and 29.48 mm). It is interesting to note that the mean compactness for four lesions monotonically increases, indicating that the IAC lesions were more compact than the other three lesions.

The texture of the segmented lesions was quantified using the GLCM. The GLCM describes the second-order joint probability function of an image where the (i, j) element of the GLCM indicates the number of times the gray levels i and j occur at a specific pixel distance in a particular direction. The variance and the autocorrelation of the GLCM matrix show significant differences among the four lesion groups. The texture of the segmented lesion is also quantified in terms of the GLRL matrix. The element (i, j) of the GLRL matrix represents the number of times (j) that a signal intensity value (i) occurs consecutively in a specified direction. The short-run emphasis (SRE) computed from the GLRL matrix measures the distribution of short runs, which indicates small structures with similar signal intensity values. The higher the SRE, the finer the structures. SRE is not a statistically significant parameter for differentiating the four lesion groups. On the other hand, the long-run emphasis (LRE) metric computes the distribution of long runs, indicating larger or coarser structures with similar signal intensity values. The LRE is a statistically significant parameter differentiating the four lesion groups. The low gray-level run emphasis metric measures the distribution of low gray levels, and the high gray-level run emphasis metric measures the distribution of higher gray level values. The low gray-level run emphasis is not a statistically significant metric that differentiates the lesions; the high gray-level run emphasis differentiates the four groups. Similarly, short-run low gray-level emphasis and short-run high gray-level emphasis quantify the joint distribution of short runs and low-level signal intensity values and short runs and high-level signal intensity values, respectively. The short-run low gray-level emphasis does not show statistically significant differences among the four groups; the short-run high gray-level emphasis does show statistically significant differences among the four groups.

The metrics for all 248 nodules for which preoperative CT scans were available are summarized in Table 2.

Statistical Analysis of Tumor Heterogeneity Metrics on Postoperative CT

On postoperative CT, 51 metrics showed significant differences among the lesion groups. SRE was the only metric that showed significance on postoperative CT but not on preoperative CT. Table 1 shows that the trend for the metrics is very similar for postoperative CT and preoperative CT. Although the metrics computed from postoperative CT showed greater significance in differentiating among the four GGN groups compared with the metrics obtained from preoperative CT, the improvement in the differential diagnosis of the nodule was minimal.

Statistical Analysis of Tumor Heterogeneity Metrics for Adenocarcinoma In Situ and Minimally Invasive Adenocarcinoma Groups

On preoperative CT, 32 of 57 metrics showed statistical significance, and on postoperative CT, 24 of 57 metrics showed statistical significance. Of the 24 metrics that showed significant differences in the lesions on postoperative CT, 19 also showed significant differences between AIS and MIA on preoperative CT. The additional metrics that showed significance on postoperative CT only and no significance on preoperative CT were median signal intensity, correlations of the GLCM matrix, high gray-level run emphasis, short-run high gray-level emphasis, and long-run high gray-level emphasis. The box plots for the representative parameters for the AIS and MIA groups are shown in Figure 3.

Statistical Analysis of Tumor Heterogeneity Metrics for Indolent and Invasive Lesions

With AAH and AIS considered indolent tumors, and with MIA and IAC considered invasive tumors, Table 3 shows the summary statistics for indolent and invasive GGNs. Significant differences between indolent and invasive carcinomas on preoperative CT were found for 53 of 57 metrics, and 51 of 57 metrics showed significant differences between the lesions on postoperative CT. The additional metrics that did not show significance on postoperative CT but showed significance on preoperative CT were minimum signal intensity and skewness. The box plots illustrating the variation of the parameters for the indolent and invasive lesion groups are shown in Figure 4.

Support Vector Machine and Manual Classification of Ground-Glass Opacity Nodules

As shown by the previously stated results, although there are a number of features that show differences among the four GGN classes, there is significant overlap in the metrics for the four classes, thereby preventing an accurate and robust choice of thresholds for classifying the GGNs. An SVM has been trained with all the heterogeneity metrics obtained on preoperative CT to distinguish between the different groups of lesions. The accuracy in predicting lesion types is summarized in Table 4.

All four classes—The SVM was trained with 76% of the total samples (188/248). The SVM was trained using a leave-one-out strategy. The optimal parameters (C, γ) were 2 and 0.125, respectively. The trained SVM was then tested on the remainder of the samples. The accuracy of predicting the lesion type was 70.9%.

Adenocarcinoma in situ and minimally invasive adenocarcinoma lesions—When only AIS and MIA lesions were considered, the accuracy in predicting lesions was 73.1%. For cases that were misclassified, the AIS lesions were misclassified as MIA, and MIA lesions were misclassified as IAC lesions. None of the AIS or MIA lesions was misclassified as less invasive nodules.

Indolent and invasive lesions—Similar to the aforementioned procedure, an SVM was trained for classifying indolent and invasive lesions. The size of the training set was 188 samples (76% of the total size), with 13 AAH and 56 AIS lesions constituting the indolent set and with 74 MIA and 45 IAC lesions constituting the invasive lesion set. The optimal parameters (C, γ) were 4 and 0.125. The trained SVM was tested on the remainder of the samples. The accuracy of the SVM in classifying indolent and invasive lesions was 88.1%.

Manual classification of the lesions—Three expert radiologists (radiologist 1, who had 12 years' experience; radiologist 2, who had 10 years' experience; and radiologist 3, who had 1 year of experience) classified the lesions on preoperative CT and postoperative CT on the basis of the new classifications of lung adenocarcinomas published in 2011 [3]. The mean accuracy in classifying all four lesions was 42.1% on preoperative CT and 39.9% on postoperative CT. The accuracy of the radiologists in classifying AIS and MIA lesions on preoperative and postoperative CT was 35.0% and 29.7%, respectively. Their accuracy in predicting indolent and invasive lesions on preoperative CT and postoperative CT was 64.5% and 63.4%, respectively. The interrater agreement based on the Fleiss kappa statistics was 0.0886 for classifying all the lesions, which corresponded to a poor level of agreement.

Discussion

In 2011, a new international multidisciplinary classification was published in the *Journal of Thoracic Oncology* under the sponsorship of the American Thoracic Society, the International Association for the Study of Lung Cancer, and the European Respiratory Society [3]. The primary motivation for this classification was to address the confusion resulting from the previous World Health Organization classification in which the term "bronchioloalveolar carcinoma (BAC)" was used to describe widely divergent tumors on the basis of clinical, radiologic, pathologic, and molecular subtypes of tumors. According to the new classifications, lung adenocarcinomas were to be primarily classified as follows: AAH is smaller than 5 mm and has no invasion, AIS is smaller than 30 mm and has no invasion, MIA is larger than 30 mm and has an invasive component smaller than 5 mm, and IAC has an invasive component larger than 5 mm. However, this classification was primarily based on the measurement of pathologic samples. It is not clear how the size criterion for classifying lesions translates to imaging findings on lung CT images. What makes it more challenging for a radiologist is that a pure GGN on CT can manifest as either indolent or invasive cancer. Jin et al. [20] reported that nearly 40% of pure GGNs in their study were invasive adenocarcinomas. This underscores the importance for developing a better understanding of the appearance of GGNs on CT by using quantitative analysis to aid in determining a differential diagnosis.

With the advent of lung cancer screening for smokers and the detection of early-stage lung cancers smaller than 2 cm, it is imperative to understand how these nodules can be classified on diagnostic CT images, to aid decisions regarding the surgical approach. Recent studies have suggested that sublobar resection for pure AIS smaller than 2 cm yields disease-free survival and recurrence rates comparable to those of lobectomy. However, lobectomy is still considered the standard of care for lesions smaller than 2 cm with an invasive component (MIA or IAC) [21]. For limited resections to be oncologically valid, a precise preoperative diagnosis becomes imperative.

Several groups have developed computerized methods for classifying GGNs. Nine unique examples that describe the lesions have been developed using an unsupervised clustering technique [22]. The voxels within the lesion were compared with the nine exemplars, and the resultant color map was used to classify the voxels. A similar clustering-based algorithm was used to classify the GGNs [23]. Patel et al. [24] described a practical algorithmic approach for differentiating solitary pulmonary nodules on the basis of the morphologic characteristics of the lesion. Texture analysis based on PET/CT images was used to predict the survival of patients with non–small cell lung cancer [25].

In the present study, we developed an SVM-based machine-learning algorithm that learns the imaging characteristics of the four types of GGNs: AAH, AIS, MIA, and IAC. The imaging characteristics define the morphologic, shape, and texture features of GGNs with the use of 57 different metrics. To our knowledge, this is the first study that has exhaustively investigated the different features of GGNs. The imaging features have been quantified using an open-source software module, allowing other research groups to test and validate the imaging biomarkers for classifying GGNs.

In accordance with the 2011 International Association for the Study of Lung Cancer guidelines for lesion classification, the size of the GGNs, measured in terms of the volume and maximum 3D diameter, increases from AAH to IAC. However, the maximum 3D diameter of the nodules measured on preoperative CT is significantly lower than the thresholds based on pathologic imaging that are noted in the 2011 International Association for the Study of Lung Cancer guidelines. This may also explain the lower accuracy of classification of GGNs by the three radiologists, who classified the lesions on the basis of the International Association for the Study of Lung Cancer guidelines.

This study could provide the basis for a more accurate classification of GGNs on the basis of radiologic findings on high-resolution diagnostic CT examinations. One surprising result was that the compactness of the nodules monotonically increased from AAH to IAC, indicating that IAC lesions were more compact than AAH nodules. This was further confirmed by the ratio of surface area to volume, which monotonically decreased from the AAH category to the IAC category. As expected, the mean signal intensity of the lesions increased from AAH to IAC nodules because of the increased size of the solid component within the nodule, a finding that was also confirmed by Ikeda et al. [26]. Mean entropy increased from AAH to IAC nodules because of the increased disorder in the lesion structure with increasing invasiveness, as was also found by Son et al. [27]. LRE, which quantifies the texture of coarser structures within the nodule, shows significant differences between the nodules, whereas SRE, which quantifies texture of finer structures, does not show statistically significant differences among the four lesion categories on preoperative CT. This could be because CT has insufficient resolution to delineate the finer structures within the nodule and because it can only detect changes in coarser structures within the lesion. The texture metric high gray-level run emphasis, which measures the distribution of higher gray levels, shows statistically significant differences among the four GGN categories; low gray-level run emphasis shows no difference. This can be explained by a gradual increase in the size of the solid component from AAH to IAC nodules, which is reflected in the change in the high-signal-intensity gray levels. For the same reason, short-run low gray-level emphasis does not show significant differences, whereas short-run high gray-level emphasis shows significant differences between the four GGN groups.

One of the objectives of this study was to evaluate the use of iodinated contrast medium for improving the differential diagnoses of GGNs. The number of heterogeneity metrics that showed significant differences among the four GGN categories was similar (50 metrics on preoperative CT and 51 metrics on postoperative CT images), although the metrics showed a stronger statistical significance of differentiation among the four groups on postoperative CT images. For differentiation between AIS and MIA, the number of metrics that showed significant differences between the two groups was higher with the use of preoperative versus postoperative CT images. The same was true for differentiating between indolent and invasive carcinomas. The accuracy of the three radiologists in predicting lesions using postoperative CT images was comparable to the prediction using preoperative CT images, suggesting that contrast enhancement does not significantly improve the differential diagnoses of GGNs and that it is not necessary to expose patients to additional radiation to improve the accuracy of classifying GGNs. However, other groups have shown the utility of a different approach using dynamic first-pass perfusion CT on a multidetector scanner to differentiate between benign and malignant solitary pulmonary nodules [28–31]. Parameters such as mean perfusion, peak enhancement intensity, and blood volume were shown to be significantly lower in value for benign tumors than for malignant tumors. However, we did not address the perfusion of contrast medium into the GGNs, and we studied only the structural heterogeneity of the tumors on preoperative CT and postoperative CT.

The present study has several limitations. The most significant limitation was that segmentation of the lesions was done manually, and in many of the cases, it was difficult to exclude vessels or other structures that may have appeared as a solid component with the lesion. This could be one of the primary reasons for the SVM misclassifying GGNs as more invasive lesions. In addition, it was difficult to accurately delineate the spiculations of the nodule, which could explain the reason for the increasing compactness of the nodules as the invasiveness of the nodules increased. There were also significantly fewer AAH lesions that were analyzed as part of this study, making it difficult to quantify the range of imaging metrics for AAH lesions. The quantitative metrics are also dependent on the CT acquisition parameters, making it imperative to standardize the acquisition protocol to enable uniform measurements across institutions.

Compared with the GGN classification done by the three radiologists, the SVM trained using all the heterogeneity features showed significantly higher accuracy in classifying the lesions into the four groups, differentiating between AIS and MIA and between indolent and invasive lesions. The high accuracy achieved by the SVM could provide radiologists a second-read option for reliably assessing the cancer risk of lesions and to improve interobserver agreement [32]. In addition, the prediction of malignancy risk by the SVM could also provide the surgeon with confidence in choosing an optimal therapeutic option.

Acknowledgments

Supported by grants P41EB015898 and P41RR019703 from the National Center for Research Resources and the National Institute of Biomedical Imaging and Bioengineering of the National Institutes of Health.

References

1. National Lung Screening Trial Research Team. Aberle DR, Adams AM, Berg CD, et al. Reduced lung-cancer mortality with low-dose computed tomographic screening. N Engl J Med. 2011; 365:395–409. [PubMed: 21714641]
2. Oken MM, Hocking WG, Kvale PA, et al. Screening by chest radiograph and lung cancer mortality: the Prostate, Lung, Colorectal, and Ovarian (PLCO) randomized trial. JAMA. 2011; 306:1865–1873. [PubMed: 22031728]
3. Travis WD, Brambilla E, Noguchi M, et al. International Association for the Study of Lung Cancer/American Thoracic Society/European Respiratory Society international multidisciplinary classification of lung adenocarcinoma. J Thorac Oncol. 2011; 6:244–285. [PubMed: 21252716]
4. Travis WD, Brambilla E, Van Schil P, et al. Paradigm shifts in lung cancer as defined in the new IASLC/ATS/ERS lung adenocarcinoma classification. Eur Respir J. 2011; 38:239–243. [PubMed: 21804158]
5. Travis WD, Brambilla E, Riely GJ. New pathologic classification of lung cancer: relevance for clinical practice and clinical trials. J Clin Oncol. 2013; 31:992–1001. [PubMed: 23401443]
6. Watanabe S, Watanabe T, Arai K, Kasai T, Haratake J, Urayama H. Results of wedge resection for focal bronchioloalveolar carcinoma showing pure ground-glass attenuation on computed tomography. Ann Thorac Surg. 2002; 73:1071–1075. [PubMed: 11996243]
7. Vazquez M, Carter D, Brambilla E, et al. Solitary and multiple resected adenocarcinomas after CT screening for lung cancer: histopathologic features and their prognostic implications. Lung Cancer. 2009; 64:148–154. [PubMed: 18951650]
8. Borczuk AC, Qian F, Kazeros A, et al. Invasive size is an independent predictor of survival in pulmonary adenocarcinoma. Am J Surg Pathol. 2009; 33:462–469. [PubMed: 19092635]
9. Yim J, Zhu LC, Chiriboga L, Watson HN, Goldberg JD, Moreira AL. Histologic features are important prognostic indicators in early stages lung adenocarcinomas. Mod Pathol. 2007; 20:233–241. [PubMed: 17192789]
10. Suzuki K, Koike T, Asakawa T, et al. A prospective radiological study of thin-section computed tomography to predict pathological noninvasiveness in peripheral clinical IA lung cancer (Japan Clinical Oncology Group 0201). J Thorac Oncol. 2011; 6:751–756. [PubMed: 21325976]
11. Godoy MCB, Naidich DP. Overview and strategic management of subsolid pulmonary nodules. J Thorac Imaging. 2012; 27:240–248. [PubMed: 22847591]

12. Godoy MCB, Naidich DP. Subsolid pulmonary nodules and the spectrum of peripheral adenocarcinomas of the lung: recommended interim guidelines for assessment and management. Radiology. 2009; 253:606–622. [PubMed: 19952025]
13. Naidich DP, Bankier AA, MacMahon H, et al. Recommendations for the management of subsolid pulmonary nodules detected at CT: a statement from the Fleischner Society. Radiology. 2013; 266:304–317. [PubMed: 23070270]
14. MacMahon H, Bankier AA, Naidich DP. Lung cancer screening: what is the effect of using a larger nodule threshold size to determine who is assigned to short-term CT follow-up? Radiology. 2014; 273:326–327. [PubMed: 25340268]
15. Fedorov A, Beichel R, Kalpathy-Cramer J, et al. 3D Slicer as an image computing platform for the Quantitative Imaging Network. Magn Reson Imaging. 2012; 30:1323–1341. [PubMed: 22770690]
16. Slicer website. www.slicer.org/wiki/Documentation/Nightly/Modules/HeterogeneityCAD. Accessed October 5, 2017
17. Cortes C, Vapnik V. Support-vector networks. Mach Learning. 1995; 20:273–297.
18. Burges CJC. A tutorial on support vector machines for pattern recognition. Data Min Knowl Discov. 1998; 2:121–167.
19. Chang CC, Lin CJ. LIBSVM: a library for support vector machines. ACM Transactions on Intelligent Systems and Technology. 2011; 2:1–27.
20. Jin X, Zhao S-H, Gao J, et al. CT characteristics and pathological implications of early stage (T1N0M0) lung adenocarcinoma with pure ground-glass opacity. Eur Radiol. 2015; 25:2532–2540. [PubMed: 25725775]
21. Van Schil PE, Asamura H, Rusch VW, et al. Surgical implications of the new IASLC/ATS/ERS adenocarcinoma classification. Eur Respir J. 2012; 39:478–486. [PubMed: 21828029]
22. Maldonado F, Boland JM, Raghunath S, et al. Noninvasive characterization of the histopathologic features of pulmonary nodules of the lung adenocarcinoma spectrum using computer-aided nodule assessment and risk yield (CANARY): a pilot study. J Thorac Oncol. 2013; 8:452–460. [PubMed: 23486265]
23. Pires, A., Rusinek, H., Suh, J., Naidich, DP., Pass, H., Ko, JP. Clustering of lung adenocarcinomas classes using automated texture analysis on CT images. SPIE Digital Library website. www.spiedigitallibrary.org/conference-proceedings-of-spie/8669/1/Clustering-of-lung-adenocarcinomas-classes-using-automated-texture-analysis-on/10.1117/12.2007154.short?SSO=1. Published March 13, 2013. Accessed August 24, 2017
24. Patel VK, Naik SK, Naidich DP, et al. A practical algorithmic approach to the diagnosis and management of solitary pulmonary nodules. Part 2. Pretest probability and algorithm. Chest. 2013; 143:840–846. [PubMed: 23460161]
25. Ganeshan B, Panayiotou E, Burnand K, Dizdarevic S, Miles K. Tumour heterogeneity in non-small cell lung carcinoma assessed by CT texture analysis: a potential marker of survival. Eur Radiol. 2012; 22:796–802. [PubMed: 22086561]
26. Ikeda K, Awai K, Mori T, Kawanaka K, Yamashita Y, Nomori H. Differential diagnosis of ground-glass opacity nodules: CT number analysis by three-dimensional computerized quantification. Chest. 2007; 132:984–990. [PubMed: 17573486]
27. Son JY, Lee HY, Lee KS, et al. Quantitative CT analysis of pulmonary ground-glass opacity nodules for the distinction of invasive adenocarcinoma from pre-invasive or minimally invasive adenocarcinoma. PLoS One. 2014; 9:e104066. [PubMed: 25102064]
28. Li Y, Yang ZG, Chen TW, Yu JQ, Sun JY, Chen HJ. First-pass perfusion imaging of solitary pulmonary nodules with 64-detector row CT: comparison of perfusion parameters of malignant and benign lesions. Br J Radiol. 2010; 83:785–790. [PubMed: 20647512]
29. Miles KA. Perfusion CT for the assessment of tumour vascularity: which protocol? Br J Radiol. 2003; 76:S36–S42. [PubMed: 15456712]
30. Ohno Y, Koyama H, Matsumoto K, et al. Differentiation of malignant and benign pulmonary nodules with quantitative first-pass 320-detector row perfusion CT versus FDG PET/CT. Radiology. 2011; 258:599–609. [PubMed: 21273522]
31. Tacelli N, Remy-Jardin M, Copin M-C, et al. Assessment of non-small cell lung cancer perfusion: pathologic-CT correlation in 15 patients. Radiology. 2010; 257:863–871. [PubMed: 20843993]

32. Jeon KN, Goo JM, Lee CH, et al. Computer-aided nodule detection and volumetry to reduce variability between radiologists in the interpretation of lung nodules at low-dose screening computed tomography. Invest Radiol. 2012; 47:457–461. [PubMed: 22717879]

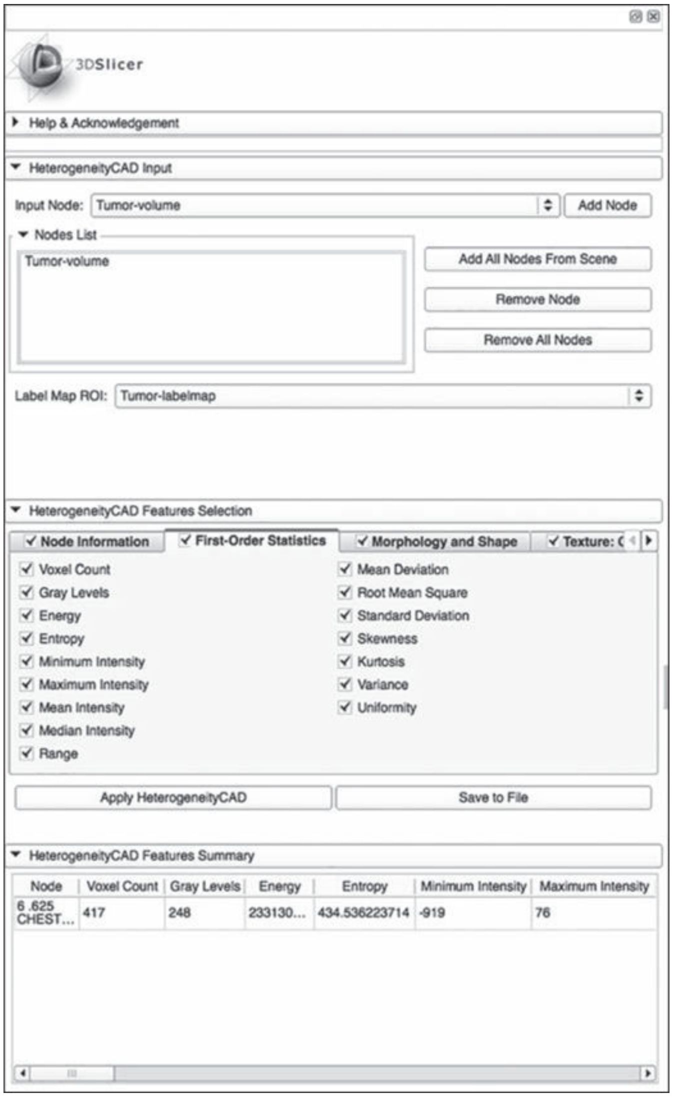

Input Node: Tumor-volume

Nodes List

Tumor-volume

Label Map ROI: Tumor-labelmap

☑ Voxel Count
☑ Gray Levels
☑ Energy
☑ Entropy
☑ Minimum Intensity
☑ Maximum Intensity
☑ Mean Intensity
☑ Median Intensity
☑ Range
☑ Mean Deviation
☑ Root Mean Square
☑ Standard Deviation
☑ Skewness
☑ Kurtosis
☑ Variance
☑ Uniformity

Node	Voxel Count	Gray Levels	Energy	Entropy	Minimum Intensity	Maximum Intensity
6 .625 CHEST...	417	248	233130...	434.536223714	-919	76

Fig. 1.

Graphic user interface for module used in image processing and navigation software (3D Slicer, version 4.3.0, Brigham and Women's Hospital).

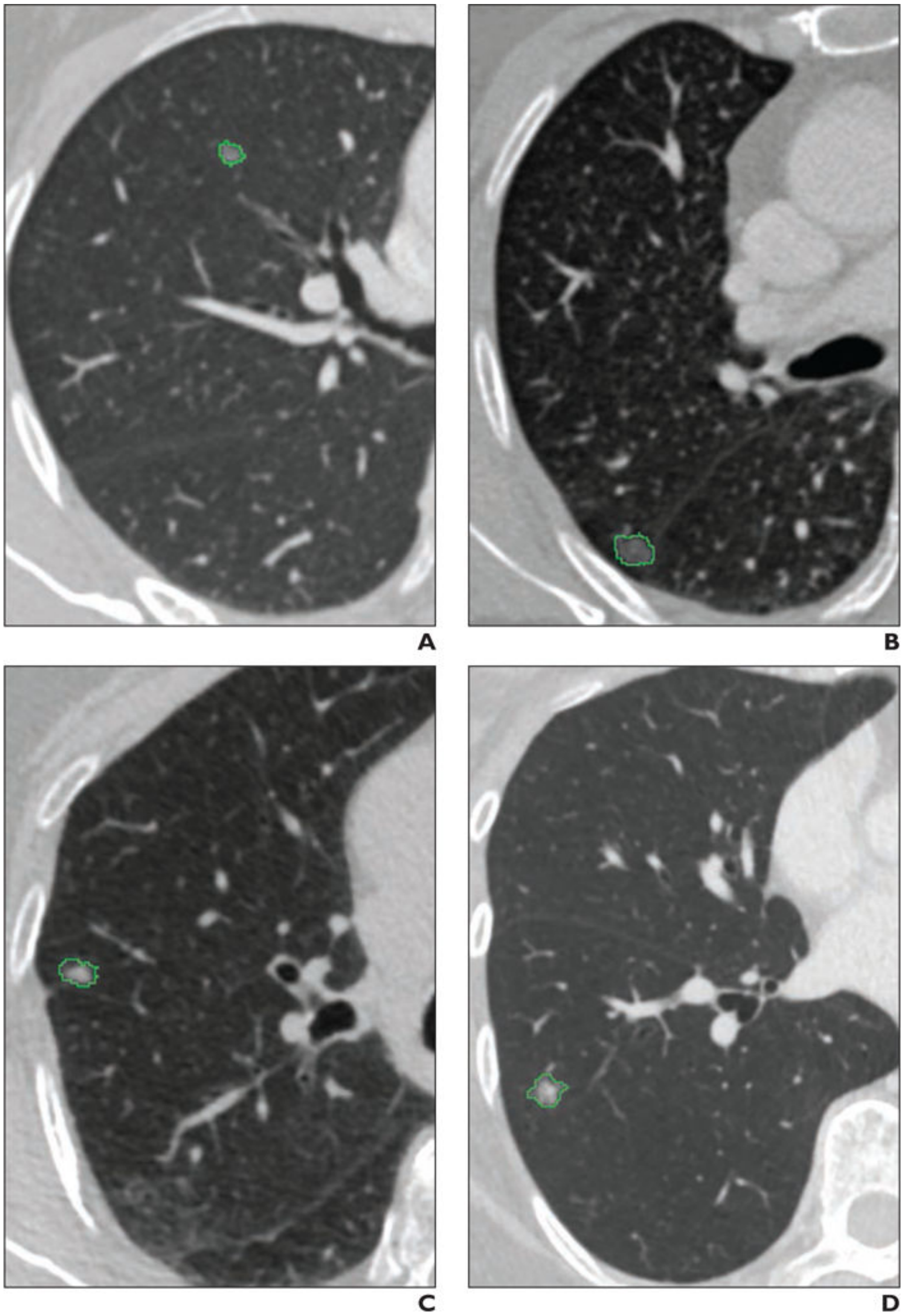

Fig. 2.

Preoperative CT scans of four types of ground-glass opacity nodules (GGNs). GGNs have been segmented on CT images. Segmentation outline is shown in green.

A–D, CT scans show atypical adenomatous hyperplasia (**A**), adenocarcinoma in situ (**B**), minimally invasive adenocarcinoma (**C**), and invasive adenocarcinoma (**D**).

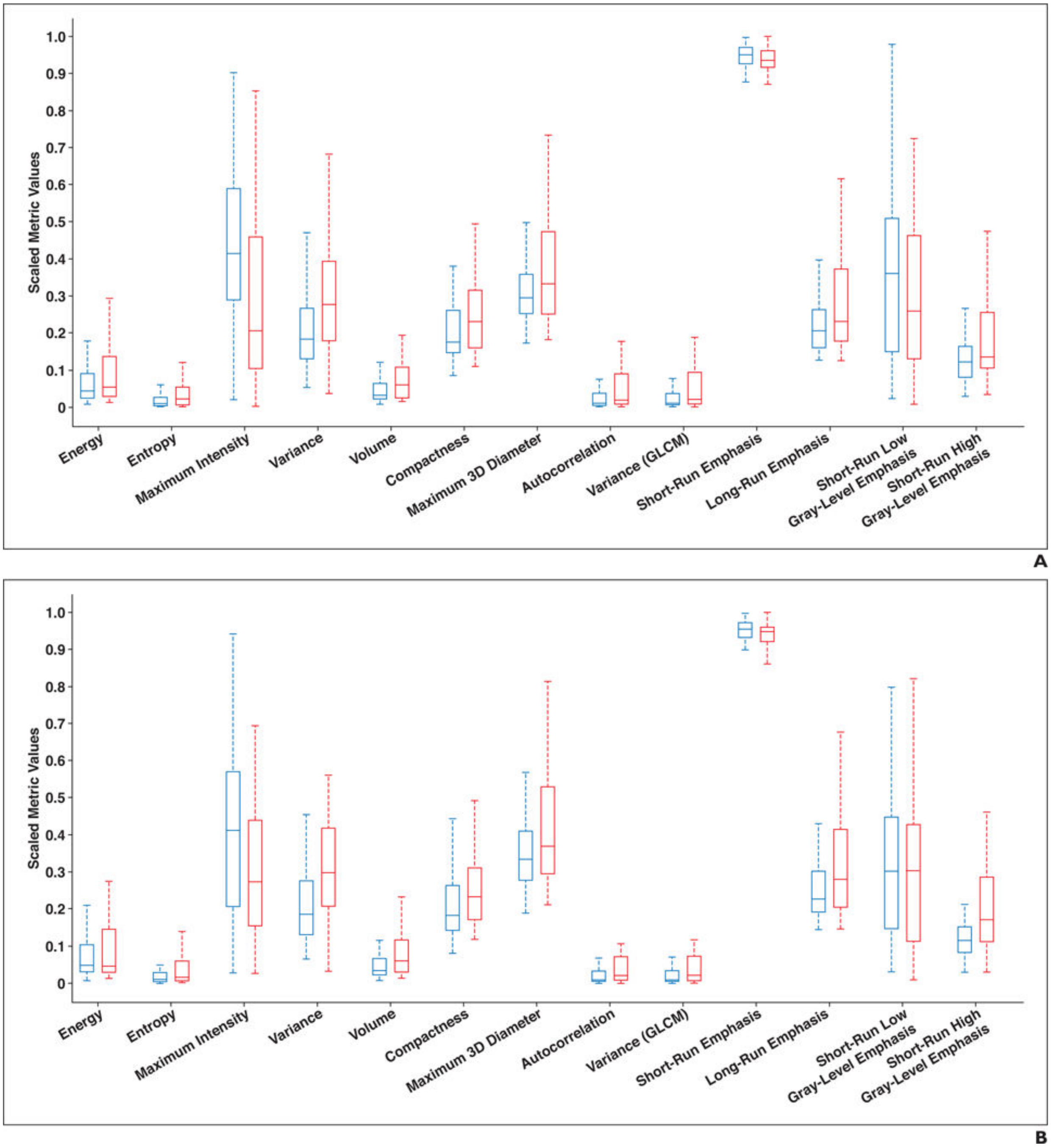

Fig. 3.

Box plots of representative metrics for adenocarcinoma in situ (*blue*) and minimally invasive adenocarcinoma (*red*) lesions on preoperative (**A**) and postoperative (**B**) CT scans. Horizontal lines within boxes denote mean values, and vertical lines and whiskers denote 95% CIs. GLCM = gray-level co-occurrence matrix.

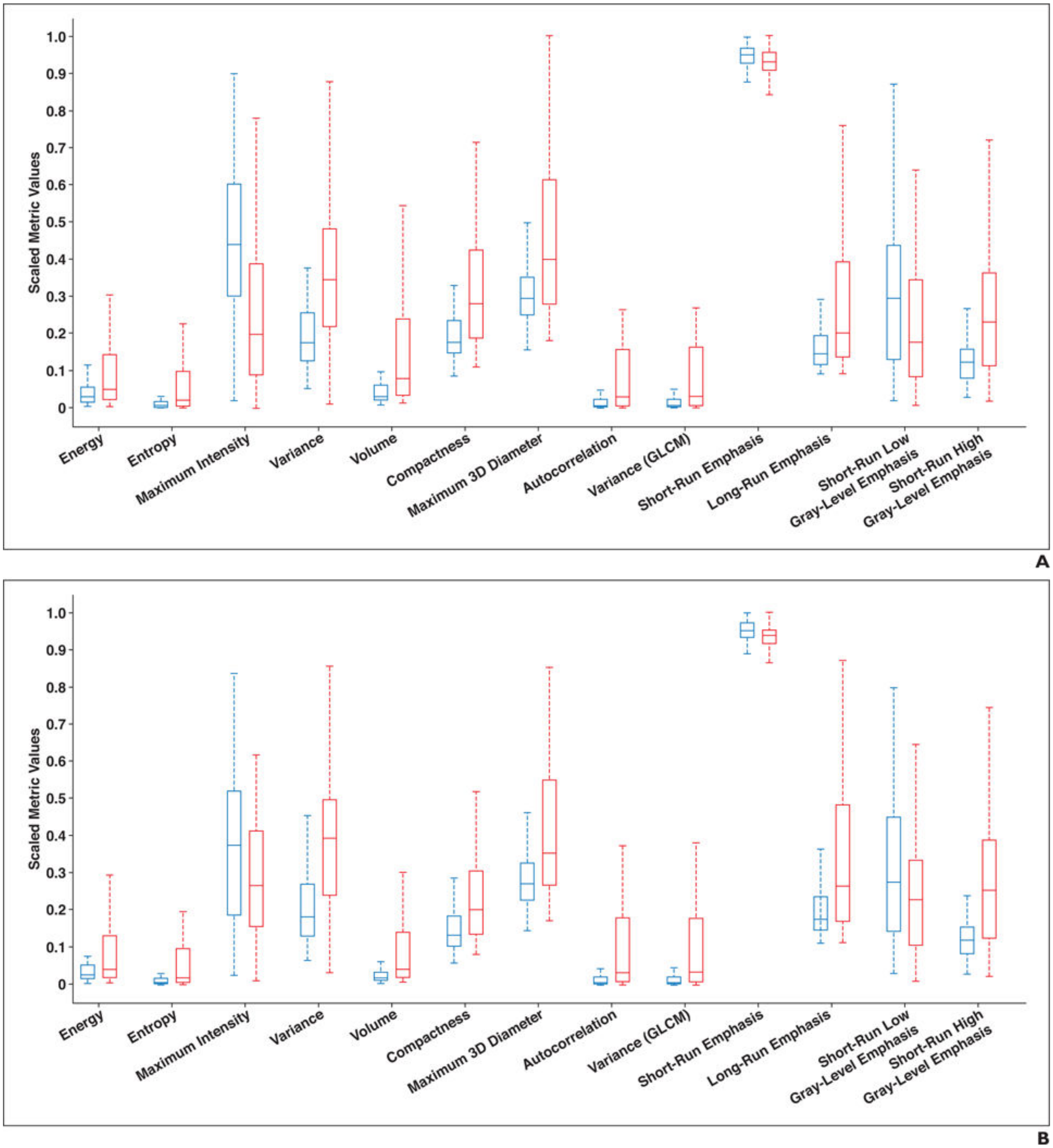

Fig. 4.

Box plots showing representative metrics for indolent (*blue*) and invasive (*red*) lesions on preoperative (**A**) and postoperative (**B**) CT scans. Horizontal lines within boxes denote mean values, and vertical lines and whiskers denote 95% CIs. GLCM = gray-level co-occurrence matrix.

TABLE 1

Summary Statistics for the Four Ground-Glass Opacity Nodule (GGN) Categories on Preoperative and Postoperative CT Scans

	Preoperative CT Scans					Postoperative CT Scans				
Metric	**AAH**	**AIS**	**MIA**	**IAC**	**p**	**AAH**	**AIS**	**MIA**	**IAC**	**p**
Minimum signal intensity (HU)	−805.3 ± 67.6	−806.3 ± 74.3	−785.7 ± 75.0	−736.6 ± 159.6	0.08	−804.7 ± 71.7	−803.9 ± 61.5	−786.0 ± 76.4	−776.4 ± 100.1	0.31
Maximum signal intensity (HU)	−308.4 ± 150.0	−228.3 ± 177.3	−113.7 ± 206.0	17.9 ± 161.5	1.6 × 10^{-1}[a]	−200.43 ± 231.68	−181.76 ± 188.79	−40.897 ± 197.06	121.7 ± 192.41	5.53 × 10^{-8}[a]
Mean signal intensity (HU)	−633.1 ± 52.6	−613.1 ± 88.2	−585.8 ± 84.6	−491.2 ± 154.6	6.9 × 10^{-5}[a]	−612.31 ± 64.868	−595.45 ± 90.414	−549.55 ± 90.894	−476.5 ± 131.77	6.67 × 10^{-5}[a]
Skewness	0.56 ± 0.42	0.60 ± 0.51	0.90 ± 0.68	0.71 ± 0.45	0.14	0.59 ± 0.54	0.59 ± 0.44	0.76 ± 0.51	0.73 ± 0.49	0.31
Kurtosis	0.26 ± 1.61	0.33 ± 1.63	0.96 ± 2.85	0.09 ± 1.09	0.65	0.54 ± 2.53	0.14 ± 1.27	0.43 ± 1.59	0.18 ± 1.14	0.84
Variance in signal intensity	8841 ± 1794	13,679 ± 9653	19,115 ± 11,029	27,319 ± 13,149	1.6 × 10^{-6}[a]	12,069 ± 2886.9	16,224 ± 11,161	23,309 ± 11,581	34,870 ± 13,908	4.25 × 10^{-8}[a]
Energy	3.4 × 108 ± 2.85 × 108	4.24 × 10^{8} ± 4.92 × 10^{8}	7.23 × 10^{8} ± 1.03 × 10^{9}	1.59 × 10^{9} ± 2.17 × 10^{9}	0.035[a]	3.94 × 10^{8} ± 3.38 × 10^{8}	4.36 × 10^{8} ± 4.86 × 10^{8}	7.01 × 10^{8} ± 1.00 × 10^{9}	1.70 × 10^{9} ± 2.28 × 10^{9}	0.026[a]
Entropy	1772.7 ± 2278.4	2696 ± 5085.9	6081 ± 13,754	22,019 ± 32,518	2.1 × 10^{-4}[a]	2092.1 ± 2916.3	2852.7 ± 5158.3	6231.3 ± 13,848	22,500 ± 35,029	2.07 × 10^{-4}[a]
Volume (mL)	0.43 ± 0.45	0.53 ± 0.68	0.94 ± 1.45	2.10 ± 1.99	8.2 × 10^{-6}[a]	0.51 ± 0.57	0.57 ± 0.71	1.00 ± 1.49	2.73 ± 3.46	1.22 × 10^{-5}[a]
Surface area (mm^2)	483.8 ± 384.0	579.2 ± 529.2	888.7 ± 915.2	1772.6 ± 1419.1	1.7 × 10^{-5}[a]	533.9 ± 425.2	601.8 ± 547.7	924.1 ± 916.9	2023.3 ± 1845.8	1.11 × 10^{-5}[a]
Compactness	3.5 ± 1.6	3.6 ± 1.9	4.6 ± 2.8	7.0 ± 3.3	7.7 × 10^{-6}[a]	3.7 ± 1.9	3.8 ± 2.0	4.8 ± 2.8	7.8 ± 4.8	1.74 × 10^{-5}[a]
Maximum 3D diameter (mm)	12.0 ± 4.4	13.7 ± 5.7	16.1 ± 7.5	22.5 ± 9.3	8.2s × 10^{-5}[a]	13.0 ± 4.8	13.9 ± 5.5	16.4 ± 7.3	23.4 ± 9.8	4.76 × 10^{-5}[a]
Spheric disproportion	2.03 × 10^{-3} ± 2.35 × 10^{-3}	1.91 × 10^{-3} ± 1.80 × 10^{-3}	1.19 × 10^{-3} ± 1.15 × 10^{-3}	5.10 × 10^{-4} ± 8.27 × 10^{-4}	6.8 × 10^{-6}[a]	1.89 × 10^{-3} ± 2.33 × 10^{-3}	1.76 × 10^{-3} ± 1.79 × 10^{-3}	1.05 × 10^{-3} ± 9.76 × 10^{-4}	4.87 × 10^{-4} ± 7.87 × 10^{-4}	1.17 × 10^{-5}[a]
Autocorrelation	1.89 × 10^{7} ± 1.73 × 10^{7}	3.72 × 10^{7} ± 8.08 × 10^{7}	8.50 × 10^{7} ± 1.72 × 10^{8}	3.45 × 10^{8} ± 4.35 × 10^{8}	3.2 × 10^{-6}[a]	3.05 × 10^{7} ± 2.94 × 10^{7}	4.88 × 10^{7} ± 1.07 × IO^{8}	1.13 × 10^{8} ± 2.26 × 10^{8}	5.24 × 10^{8} ± 6.42 × 10^{8}	8.47 × 10^{-7}[a]
Cluster prominence	1.52 × 10^{13} ± 1.55 × 10^{13}	9.67 × 10^{13} ± 4.58 × 10^{14}	1.82 × 10^{14} ± 3.70 × 10^{14}	1.16 × 10^{15} ± 1.73 10^{15}	5.6 × 10^{-6}[a]	3.57 × 10^{13} ± 3.90 × 10^{13}	1.53 × 10^{14} ± 7.16 × 10^{14}	2.94 × $10^{,14}$ ± 5.99 × 10^{14}	2.37 × 10^{15} ± 3.39 × 10^{15}	1.62 × 10^{-7}[a]
Cluster shade	3.28 × 10^{10} ± 3.13 × 10^{10}	1.06 × 10^{11} ± 3.67 × 10^{11}	2.28 × 10^{11} ± 4.48 × 10^{11}	1.15 × 10^{12} ± 1.55 × 10^{12}	6.8 × 10^{-6}[a]	6.36 × 10^{10} ± 6.49 × 10^{10}	1.53 × 10^{11} ± 5.28 × 10^{11}	3.37 × 10^{11} ± 6.63 × 10^{11}	2.04 × 10^{12} ± 2.65 × 10^{12}	2.99 × 10^{-7}[a]
Cluster tendency	7.71 × 10^{7} ± 6.95 × 10^{7}	1.51 × 10^{8} ± 3.32 × 10^{8}	3.36 × 10^{8} ± 6.37 × 10^{8}	1.32 × 10^{9} ± 1.63 × 10^{9}	5.9 × 10^{-6}[a]	1.24 × 10^{8} ± 1.19 × 10^{8}	1.99 × 10^{8} ± 4.39 × 10^{8}	4.49 × 10^{8} ± 8.53 × 10^{8}	2.05 × 10^{9} ± 2.45 × 10^{9}	7.36 × 10^{-7}[a]
Homogeneity	35.9 ± 29.4	42.6 ± 55.9	70.8 ± 112.5	210.6 ± 290.1	2.8 × 10^{-4}[a]	38.9 ± 34.2	43.6 ± 52.4	69.0 ± 110.5	193.9 ± 269.9	2.80 × 10^{-4}[a]
Variance (GLCM)	2.09 × 10^{7} ± 1.92 × 10^{7}	4.11 × 10^{7} ± 8.88 × 10^{7}	9.37 × 10^{7} ± 1.85 × 10^{8}	3.72 × 10^{8} ± 4.64 × 10^{8}	3.1 × 10^{-6}[a]	3.34 × 10^{7} ± 3.26 × 10^{7}	5.39 × 10^{7} ± 1.17 × 10^{8}	1.24 × 10^{8} ± 2.43 × 10^{8}	5.64 × 108 ± 6.85 × 10^{8}	9.1 × 10^{-7}[a]
Short-run emphasis	9.16 × 10^{-1} ±	9.25 × 10^{-1} ±	9.14 × 10^{-1} ±	9.05 × 10^{-1} ±	0.065	9.23 × 10^{-1} ±	9.22 × 10^{-1} ±	9.14 × 10^{-1} ±	9.01 × 10^{-1} ±	0.008[a]

Metric	Preoperative CT Scans					Postoperative CT Scans				
	AAH	**AIS**	**MIA**	**IAC**	**p**	**AAH**	**AIS**	**MIA**	**IAC**	**p**
	3.13×10^{-2}	2.89×10^{-2}	3.26×10^{-2}	3.07×10^{-2}		3.29×10^{-2}	2.31×10^{-2}	2.95×10^{-2}	2.45×10^{-2}	
Long-run emphasis	2.23 ± 1.08	2.21 ± 1.32	3.06 ± 2.26	4.61 ± 3.01	1.9×10^{-4a}	2.19 ± 1.04	2.16 ± 1.03	3.00 ± 1.97	4.44 ± 2.47	1.95×10^{-5a}
Gray-level nonuniformity	3.66 ± 2.24	4.18 ± 4.30	6.16 ± 7.36	14.86 ± 21.56	2.2×10^{-3a}	3.68 ± 2.43	4.07 ± 3.85	5.66 ± 6.60	11.40 ± 12.89	0.0027^{a}
Low gray-level run emphasis	$4.70 \times 10^{-3} \pm 4.83 \times 10^{-3}$	$5.31 \times 10^{-3} \pm 3.55 \times 10^{-3}$	$4.72 \times 10^{-3} \pm 3.58 \times 10^{-3}$	$3.75 \times 10^{-3} \pm 3.87 \times 10^{-3}$	0.148	$3.47 \times 10^{-3} \pm 2.80 \times 10^{-3}$	$4.18 \times 10^{-3} \pm 2.75 \times 10^{-3}$	$4.19 \times 10^{-3} \pm 3.21 \times 10^{-3}$	$2.83 \times 10^{-3} \pm 1.97 \times 10^{-3}$	0.194
High gray-level run emphasis	$2.38 \times 10^{4} \pm 9.68 \times 10^{3}$	$2.98 \times 10^{4} \pm 2.98 \times 10^{3}$	$3.68 \times 10^{4} \pm 2.32 \times 10^{4}$	$7.13 \times 10^{4} \pm 3.99 \times 10^{4}$	9.4×10^{-6a}	$3.24 \times 10^{4} \pm 1.48 \times 10^{4}$	$3.47 \times 10^{4} \pm 3.41 \times 10^{4}$	$4.64 \times 10^{4} \pm 2.79 \times 10^{4}$	$9.71 \times 10^{4} \pm 5.36 \times 10^{4}$	5.67×10^{-8a}
Short-run low gray-level emphasis	$4.12 \times 10^{-3} \pm 4.04 \times 10^{-3}$	$4.70 \times 10^{-3} \pm 3.21 \times 10^{-3}$	$3.96 \times 10^{-3} \pm 2.97 \times 10^{-3}$	$2.99 \times 10^{-3} \pm 3.24 \times 10^{-3}$	0.065	$3.04 \times 10^{-3} \pm 2.48 \times 10^{-3}$	$3.53 \times 10^{-3} \pm 2.29 \times 10^{-3}$	$3.44 \times 10^{-3} \pm 2.58 \times 10^{-3}$	$2.14 \times 10^{-3} \pm 1.53 \times 10^{-3}$	0.061
Short-run high gray-level emphasis	$2.24 \times 10^{4} \pm 9.20 \times 10^{3}$	$2.84 \times 10^{4} \pm 2.75 \times 10^{4}$	$3.51 \times 10^{4} \pm 2.19 \times 10^{4}$	$6.82 \times 10^{4} \pm 3.83 \times 10^{4}$	7.77×10^{-6a}	$3.10 \times 10^{4} \pm 1.43 \times 10^{4}$	$3.33 \times 10^{4} \pm 3.22 \times 10^{4}$	$4.43 \times 10^{4} \pm 2.64 \times 10^{4}$	$9.26 \times 10^{4} \pm 5.10 \times 10^{4}$	6.91×10^{-8a}

Note—Except where otherwise indicated, data are mean (± SD) values. AAH = atypical adenomatous hyperplasia, AIS = adenocarcinoma in situ, MIA= minimally invasive adenocarcinoma, IAC = invasive adenocarcinoma, GLCM = gray-level co-occurrence matrix.

[a] Statistically significant.

TABLE 2

Summary Statistics for All 248 Ground-Glass Opacity Nodules on Preoperative CT

Metric	AAH	AIS	MIA	IAC	p[a]
Minimum signal intensity (HU)	−781.82 ± 54.151	−797.75 ± 78.786	−767.32 ± 78.057	−728.27 ± 114.97	1.55×10^{-4}
Maximum signal intensity (HU)	−335.53 ± 151.81	−240.64 ± 174.73	−83.566 ± 179.17	30.169 ± 147.57	4.50×10^{-18}
Mean signal intensity (HU)	−642.08 ± 61.353	−612.91 ± 85.422	−565.75 ± 86.005	−463.71 ± 134.03	1.49×10^{-14}
Skewness	0.69 ± 0.37	0.62 ± 0.49	0.83 ± 0.55	0.55 ± 0.45	5.69×10^{-3}
Kurtosis	0.28 ± 1.25	0.33 ± 1.53	0.55 ± 2.09	−0.34 ± 1.00	7.72×10^{-4}
Variance in signal intensity	8320.4 ± 4280.8	13,085 ± 9034	21,238 ± 10,731	33,858 ± 16,889	2.34×10^{-18}
Energy	$2.59 \times 10^{8} \pm 2.29 \times 10^{8}$	$3.69 \times 10^{8} \pm 4.22 \times 10^{8}$	$7.39 \times 10^{8} \pm 1.18 \times 10^{9}$	$1.09 \times 10^{9} \pm 1.62 \times 10^{9}$	5.29×10^{-4}
Entropy	1156.5 ± 1677.9	2159.3 ± 4266.8	6396.4 ± 14,683	14,345 ± 24,681	2.43×10^{-8}
Volume (mL)	0.30 ± 0.33	0.46 ± 0.57	0.98 ± 1.36	1.75 ± 1.75	3.46×10^{-13}
Surface area (mm^2)	372.84 ± 290.66	518.89 ± 454.45	948.2 ± 938.77	1578.3 ± 1372.4	3.23×10^{-13}
Compactness	2.89 ± 1.31	3.44 ± 1.68	4.70 ± 2.63	6.34 ± 2.85	5.85×10^{-13}
Maximum 3D diameter (mm)	11.01 ± 3.46	13.01 ± 4.97	16.78 ± 7.06	22.21 ± 9.57	5.72×10^{-13}
Spheric disproportion	$2.84 \times 10^{-3} \pm 2.16 \times 10^{-3}$	$2.06 \times 10^{-3} \pm 1.98 \times 10^{-3}$	$1.10 \times 10^{-3} \pm 1.10 \times 10^{-3}$	$5.14 \times 10^{-4} \pm 6.60 \times 10^{-4}$	3.36×10^{-13}
Autocorrelation	$1.05 \times 10^{7} \pm 1.35 \times 10^{7}$	$2.97 \times 10^{7} \pm 6.75 \times 10^{7}$	$1.03 \times 10^{8} \pm 2.09 \times 10^{8}$	$3.38 \times 10^{8} \pm 4.95 \times 10^{8}$	6.42×10^{-15}
Cluster prominence	$7.84 \times 10^{12} \pm 1.18 \times 10^{13}$	$6.96 \times 10^{13} \pm 3.76 \times 10^{14}$	$2.71 \times 10^{14} \pm 7.02 \times 10^{14}$	$1.49 \times 10^{15} \pm 2.91 \times 10^{15}$	1.02×10^{-15}
Cluster shade	$1.75 \times 10^{10} \pm 2.43 \times 10^{10}$	8.01 × 1010 ± 3.03 × 1011	$3.07 \times 10^{11} \pm 6.87 \times 10^{11}$	$1.32 \times 10^{12} \pm 2.25 \times 10^{12}$	2.07×10^{-15}
Cluster tendency	$4.32 \times 10^{7} \pm 5.46 \times 10^{7}$	$1.21 \times 10^{8} \pm 2.77 \times 10^{8}$	$4.07 \times 10^{8} \pm 7.94 \times 10^{8}$	$1.33 \times 10^{9} \pm 1.93 \times 10^{9}$	1.02×10^{-14}
Homogeneity	26.30 ± 23.27	36.82 ± 47.10	73.12 ± 119.98	139.67 ± 215.52	2.17×10^{-7}
Short-run emphasis	$9.26 \times 10^{-1} \pm 3.20 \times 10^{-2}$	$9.25 \times 10^{-1} \pm 2.78 \times 10^{-2}$	$9.09 \times 10^{-1} \pm 3.12 \times 10^{-2}$	$9.01 \times 10^{-1} \pm 3.03 \times 10^{-2}$	2.57×10^{-5}
Long-run emphasis	1.94 ± 0.83	2.09 ± 1.13	3.16 ± 2.16	4.50 ± 3.38	5.09×10^{-11}
Gray-level nonuniformity	3.12 ± 1.90	3.80 ± 3.63	5.97 ± 7.44	9.78 ± 15.54	1.30×10^{-4}
Low gray-level run emphasis	$7.77 \times 10^{-3} \pm 5.04 \times 10^{-3}$	$5.96 \times 10^{-3} \pm 4.22 \times 10^{-3}$	$5.12 \times 10^{-3} \pm 3.14 \times 10^{-3}$	$4.17 \times 10^{-3} \pm 2.96 \times 10^{-3}$	8.70×10^{-3}
High gray-level run emphasis	$1.60 \times 10^{4} \pm 1.01 \times 10^{4}$	$2.71 \times 10^{4} \pm 2.57 \times 10^{4}$	$4.13 \times 10^{4} \pm 2.68 \times 10^{4}$	$8.54 \times 10^{4} \pm 5.47 \times 10^{4}$	2.32×10^{-17}
Short-run low gray-level emphasis	$6.83 \times 10^{-3} \pm 4.44 \times 10^{-3}$	$5.29 \times 10^{-3} \pm 3.97 \times 10^{-3}$	$4.19 \times 10^{-3} \pm 2.64 \times 10^{-3}$	$3.25 \times 10^{-3} \pm 2.46 \times 10^{-3}$	4.77×10^{-4}
Short-run high gray-level emphasis	$1.52 \times 10^{4} \pm 9.53 \times 10^{3}$	$2.60 \times 10^{4} \pm 2.38 \times 10^{4}$	$3.96 \times 10^{4} \pm 2.57 \times 10^{4}$	$8.21 \times 10^{4} \pm 5.30 \times 10^{4}$	1.88×10^{-17}

Note—Except where otherwise indicated, data are mean (± SD) values. AAH = atypical adenomatous hyperplasia, AIS = adenocarcinoma in situ, MIA = minimally invasive adenocarcinoma, IAC = invasive adenocarcinoma.

[a] All p values were statistically significant.

TABLE 3

Summary Statistics for Indolent and Invasive Ground-Glass Opacity Nodules (GGNs) on Preoperative CT and Postoperative CT Scans

	Preoperative CT Scans			Postoperative CT Scans		
Metric	**Indolent GGNs**	**Invasive GGNs**	**p**	**Indolent GGNs**	**Invasive GGNs**	**p**
Minimum signal intensity (HU)	−806.14 ± 72.982	−765.61 ± 118.64	0.019[a]	−803.98 ± 62.152	−782.03 ± 86.265	0.059
Maximum signal intensity (HU)	−238.3 ± 174.96	−59.879 ± 198.76	6.49×10^{-7}[a]	−184.09 ± 192.36	25.621 ± 209.76	1.49×10^{-7}[a]
Mean signal intensity (HU)	−615.63 ± 84.486	−547.12 ± 126.27	8.76×10^{-5}[a]	−597.56 ± 87.321	−519.67 ± 114.39	3.06×10^{-5}[a]
Skewness	0.60 ± 0.50	0.82 ± 0.60	0.031[a]	0.59 ± 0.45	0.75 ± 0.50	0.06
Kurtosis	0.32 ± 1.62	0.60 ± 2.32	0.53	0.19 ± 1.46	0.32 ± 1.42	0.47
Variance in signal intensity	13,074 ± 9180.4	22,471 ± 12,522	2.37×10^{-6}[a]	15,705 ± 10,561	28,038 ± 13,733	9.00×10^{-8}[a]
Energy	$4.15 \times 10^{8} \pm 4.70 \times 10^{8}$	$1.08 \times 10^{9} \pm 1.64 \times 10^{9}$	0.014[a]	$4.31 \times 10^{8} \pm 4.68 \times 10^{8}$	$1.11 \times 10^{9} \pm 1.71 \times 10^{9}$	0.047[a]
Entropy	2580.6 ± 4820.4	12,601 ± 24,411	3.19×10^{-4}[a]	2757.6 ± 4920.7	12,887 ± 25,844	1.02×10^{-3}[a]
Volume (mL)	0.52 ± 0.65	1.41 ± 1.77	4.67×10^{-5}[a]	0.56 ± 0.69	1.71 ± 2.61	7.22×10^{-5}[a]
Surface area (mm^2)	567.23 ± 511.38	1250.3 ± 1219.4	9.24×10^{-5}[a]	593.33 ± 531.06	1373.8 ± 1466.6	6.77×10^{-5}[a]
Compactness	3.60 ± 1.86	5.59 ± 3.17	3.27×10^{-5}[a]	3.80 ± 1.95	6.01 ± 3.99	7.70×10^{-5}[a]
Maximum 3D diameter (mm)	13.50 ± 5.52	18.73 ± 8.81	5.29×10^{-4}[a]	13.80 ± 5.35	19.24 ± 9.02	3.39×10^{-4}[a]
Spheric disproportion	$1.92 \times 10^{-3} \pm 1.85 \times 10^{-3}$	$9.14 \times 10^{-4} \pm 1.08 \times 10^{-3}$	3.62×10^{-5}[a]	$1.78 \times 10^{-3} \pm 1.84 \times 10^{-3}$	$8.21 \times 10^{-4} \pm 9.40 \times 10^{-4}$	6.77×10^{-5}[a]
Autocorrelation	$3.49 \times 10^{7} \pm 7.60 \times 10^{7}$	$1.91 \times 10^{8} \pm 3.31 \times 10^{8}$	3.91×10^{-5}[a]	$4.65 \times 10^{7} \pm 1.01 \times 10^{8}$	$2.81 \times 10^{8} \pm 4.86 \times 10^{8}$	2.33×10^{-5}[a]
Cluster prominence	$8.66 \times 10^{13} \pm 4.29 \times 10^{14}$	$5.84 \times 10^{14} \pm 1.23 \times 10^{15}$	4.62×10^{-5}[a]	$1.38 \times 10^{14} \pm 6.70 \times 10^{14}$	$1.14 \times 10^{15} \pm 2.42 \times 10^{15}$	5.51×10^{-6}[a]
Cluster shade	$9.67 \times 10^{10} \pm 3.44 \times 10^{11}$	$6.05 \times 10^{11} \pm 1.13 \times 10^{12}$	4.77×10^{-5}[a]	$1.42 \times 10^{11} \pm 4.95 \times 10^{11}$	$1.03 \times 10^{12} \pm 1.94 \times 10^{12}$	1.03×10^{-5}[a]
Cluster tendency	$1.42 \times 10^{8} \pm 3.12 \times 10^{8}$	$7.40 \times 10^{8} \pm 1.24 \times 10^{9}$	5.33×10^{-5}[a]	$1.90 \times 10^{8} \pm 4.13 \times 10^{8}$	$1.10 \times 10^{9} \pm 1.86 \times 10^{9}$	2.22×10^{-5}[a]
Homogeneity	41.76 ± 53.14	127.99 ± 214.15	4.20×10^{-4}[a]	42.99 ± 50.27	120.09 ± 200.30	1.96×10^{-3}[a]
Variance (GLCM)	$3.86 \times 10^{7} \pm 8.34 \times 10^{7}$	$2.08 \times 10^{8} \pm 3.54 \times 10^{8}$	3.58×10^{-5}[a]	$5.13 \times 10^{7} \pm 1.10 \times 10^{8}$	$3.04 \times 10^{8} \pm 5.19 \times 10^{8}$	2.44×10^{-5}[a]
Short-run emphasis	0.92 ± 0.03	0.91 ± 0.03	1.79×10^{-2}[a]	0.92 ± 0.02	0.91 ± 0.03	5.15×10^{-3}[a]
Long-run emphasis	2.21 ± 1.28	3.70 ± 2.68	3.07×10^{-4}[a]	2.16 ± 1.02	3.59 ± 2.28	9.54×10^{-5}[a]
Gray-level nonuniformity	4.12 ± 4.09	9.72 ± 15.37	2.03×10^{-3}[a]	4.02 ± 3.69	8.01 ± 10.00	8.59×10^{-3}[a]
Low gray-level run emphasis	$5.23 \times 10^{-3} \pm 3.69 \times 10^{-3}$	$4.33 \times 10^{-3} \pm 3.70 \times 10^{-3}$	0.11	$4.09 \times 10^{-3} \pm 2.74 \times 10^{-3}$	$3.64 \times 10^{-3} \pm 2.83 \times 10^{-3}$	0.35

	Preoperative CT Scans			Postoperative CT Scans		
Metric	**Indolent GGNs**	**Invasive GGNs**	**p**	**Indolent GGNs**	**Invasive GGNs**	**p**
High gray-level run emphasis	29,001 ± 28,074	50,895 ± 35,257	1.04×10^{-4a}	34,408 ± 32,233	67,176 ± 47,244	2.83×10^{-6a}
Short-run low gray-level emphasis	$4.63 \times 10^{-3} \pm 3.29 \times 10^{-3}$	$3.56 \times 10^{-3} \pm 3.10 \times 10^{-3}$	5.06×10^{-2}	$3.47 \times 10^{-3} \pm 2.30 \times 10^{-3}$	$2.91 \times 10^{-3} \pm 2.29 \times 10^{-3}$	0.13
Short-run high gray-level emphasis	27,635 ± 25,921	48,644 ± 33,697	8.95×10^{-5a}	32,997 ± 30,451	64,024 ± 44,939	3.37×10^{-6a}

Note—Except where otherwise indicated, data are mean (± SD) values. GLCM = gray-level co-occurrence matrix.

[a] Statistically significant.

TABLE 4

Accuracy of Classification of Nodules on Preoperative CT by Three Radiologists Versus the Support Vector Machine (SVM)

Nodule Group(s)	Accuracy of Radiologists (%)	Accuracy of SVM (%)
All	39.6	70.9
AIS and MIA	35.7	73.1
Indolent and invasive	60.8	88.1

Note—AIS = adenocarcinoma in situ, MIA = minimally invasive adenocarcinoma.